

CAFlow: Adaptive-Depth Single-Step Flow Matching for Efficient Histopathology Super-Resolution

Elad Yoshai Ariel D. Yoshai
Natan T. Shaked*

School of Biomedical Engineering, Tel Aviv University, Tel Aviv, Israel

Abstract

In digital pathology, whole-slide images routinely exceed gigapixel resolution, making computationally intensive deep generative super-resolution (SR) impractical for routine deployment. Flow matching models achieve strong SR quality, but they apply the same network depth to every image, wasting computation on inputs that converge at shallow depth. We introduce CAFlow, an adaptive-depth flow matching framework that routes each image tile to the shallowest network exit that preserves reconstruction quality. CAFlow performs single-step flow matching in pixel-unshuffled rearranged space, reducing spatial computation by 16× while enabling direct inference. We show that dedicating half of training to exact $t=0$ samples is essential for single-step quality (−1.5 dB without it), a finding with practical implications for deployment since inference always operates at this timestep. The backbone, FlowResNet (1.90M parameters), mixes convolution and window self-attention blocks across four early exits spanning 3.1 to 13.3 GFLOPs. A lightweight exit classifier (~6K parameters) routes each tile to the shallowest exit that preserves quality, achieving 33% compute savings at only 0.12 dB cost. We validate clinical relevance through downstream nuclei segmentation with StarDist (Schmidt et al., 2018), confirming that SR quality preserves detection F1 score. We also show that spatially coherent whole-slide routing correlates with tissue complexity without explicit tissue-type supervision. On multi-organ histopathology ×4 SR, adaptive routing achieves 31.72 dB PSNR at 33% compute savings versus full-depth (31.84 dB), while the shallowest exit alone exceeds bicubic by +1.9 dB at 2.8× less compute than SwinIR-light (Liang et al., 2021a). The method generalizes to held-out colon tissue with minimal quality loss (−0.02 dB), and at ×8 upscaling it outperforms all comparable-compute baselines while remaining competitive with the much larger SwinIR-Medium model. The model trains in under 5 hours on a single GPU, and adaptive routing can reduce whole-slide inference from minutes to seconds, making generative SR practical for

high-throughput pathology workflows.

1 Introduction

Single-image super-resolution (SISR) is a fundamental computer vision task with particular importance in medical imaging, where high-resolution (HR) detail can be critical for diagnosis (Wang et al., 2020). Computational pathology has become increasingly important for clinical workflows (Abels et al., 2019; Baxi et al., 2024). In computational pathology, tissue specimens captured at lower magnifications or through frozen-section protocols often lack the fine-grained detail of permanent-section images, motivating ×4 super-resolution as a practical tool for improving diagnostic quality (Rivenson et al., 2019; de Haan et al., 2021; Yoshai et al., 2024).

Recent advances in generative modeling have introduced flow matching (Lipman et al., 2023; Liu et al., 2023) as a powerful framework for image restoration. Unlike diffusion models (Ho et al., 2020; Song et al., 2021) that require complex noise schedules, flow matching learns a velocity field that transports samples along straight-line paths from degraded to clean images, enabling efficient single-step inference (Lipman et al., 2023; Albergio and Vanden-Eijnden, 2023).

However, existing flow-matching SR methods apply uniform network depth to every image. This is wasteful: some images (smooth tissue backgrounds, homogeneous regions) converge after only a few residual blocks, while others (dense nuclei clusters, fine cellular structures) benefit from the full network depth including expensive attention layers. Applying the same computation to all images means that easy inputs receive unnecessary processing, inflating inference cost without improving quality.

We address this with CAFlow (Compute-Adaptive Flow matching), a framework with three contributions:

1. **Single-step flow matching in rearranged space.** Existing flow matching SR methods operate either in Variational Auto-Encoder (VAE) latent space (Wang et al., 2024) or directly at full high-resolution (HR) resolu-

*Corresponding author. Email: nshaked@tau.ac.il

tion (Saharia et al., 2022), incurring high memory and compute costs. We apply pixel-unshuffle (Shi et al., 2016) to map both the degraded and target images into a compact representation with $3s^2$ channels at $\frac{1}{s}$ the spatial resolution in each dimension, reducing the spatial compute of all network operations by $s^2=16\times$. Crucially, we show that dedicating 50% of training to exact $t=0$ samples (where t denotes the flow matching timestep that interpolates between the degraded input at $t=0$ and the target at $t=1$) is essential for single-step inference quality (-1.54 dB without it), a finding with practical implications for deployment since inference always evaluates the model at $t=0$. In practice, this means that throughout training, half of the samples in each mini-batch are drawn at exact $t=0$, with the remaining half sampled from the standard continuous timestep distribution.

2. **Graduated hybrid backbone with quality-aware routing.** FlowResNet is a 16-block network mixing FiLMResBlocks (cheap convolutions with Feature-wise Linear Modulation (FiLM) conditioning (Perez et al., 2018)) and HybridFiLMBlocks (convolution plus window self-attention (Liu et al., 2021; Liang et al., 2021a)). Hybrid blocks are concentrated in later exits, creating a graduated compute schedule from 3.1 to 13.3 giga floating-point operations (GFLOPs) ($4.3\times$ ratio). A lightweight ExitClassifier ($\sim 6K$ parameters) predicts the optimal exit from early backbone features, trained on oracle labels derived from per-exit reconstruction quality. At inference, each image is routed to its predicted exit via a single argmax , achieving 33% compute savings at 0.12 dB Peak Signal-to-Noise Ratio (PSNR) cost.
3. **Quantitative downstream validation and generalization.** We validate that SR quality translates to preserved performance in automated downstream tasks: nuclei detection using StarDist (Schmidt et al., 2018) on SR outputs preserves detection F1 score compared to HR ground truth, confirming that the reconstruction quality of CAFlow is sufficient for quantitative computational pathology workflows. Per-organ analysis across breast, kidney, and lung tissue reveals organ-specific performance variation, and whole-slide routing correlates with tissue complexity without explicit tissue-type supervision. We further demonstrate cross-organ generalization to held-out colon tissue and scaling to $\times 8$ upscaling, where CAFlow’s advantage over baselines increases.

On multi-organ histopathology $\times 4$ SR (breast, kidney, lung), adaptive routing achieves 31.72 dB at 8.9 GFLOPs (33% savings vs. full-depth 31.84 dB), while Exit 0 alone exceeds bicubic by +1.9 dB at $2.8\times$ less compute than SwinIR-light (Liang et al., 2021a).

2 Related Work

Super-Resolution in Digital Pathology Super-resolution has emerged as a practical tool in digital pathology, enabling improved visualization of tissue microstructure from lower-magnification or frozen-section acquisitions (Rivenson et al., 2019; de Haan et al., 2021; Yoshai et al., 2024). While U-Net-based architectures (Ronneberger et al., 2015) have been foundational in medical image analysis, the computational cost of modern deep generative SR models remains a barrier to large-scale adoption, particularly for whole-slide images containing hundreds to thousands of tiles per specimen.

Single Image Super-Resolution Deep learning approaches to SISR have progressed from Convolutional Neural Networks (CNNs) (He et al., 2016) (SRCNN (Dong et al., 2014), EDSR (Lim et al., 2017), RCAN (Zhang et al., 2018b)) to transformer-based models (SwinIR (Liang et al., 2021a), SRFormer (Zhou et al., 2023)). Hybrid conv + attention architectures such as Restormer (Zamir et al., 2022) and NAFNet (Chen et al., 2022) combine local convolutional processing with global attention for image restoration. Generative approaches include Generative Adversarial Networks (GAN) based methods (ESRGAN (Wang et al., 2018), Real-ESRGAN (Wang et al., 2021)), diffusion-based methods (SR3 (Saharia et al., 2022), SRDiff (Li et al., 2022), StableSR (Wang et al., 2024)), and flow-based methods (Liang et al., 2021b). All these approaches apply uniform computation across all images.

Flow Matching and Continuous Normalizing Flows Flow matching (Lipman et al., 2023) and rectified flow (Liu et al., 2023) learn a velocity field to transport distributions along optimal transport paths. Conditional flow matching (Tong et al., 2024) enables flexible conditioning mechanisms. These methods offer advantages over diffusion models in training stability and generation efficiency (Albergo and Vanden-Eijnden, 2023). A comprehensive treatment of flow matching theory and practice is provided by Lipman et al. (2024). However, existing flow matching methods use fixed-depth networks without adaptive computation.

Adaptive Computation and Early Exit Spatially adaptive computation has been explored through stochastic depth (Huang et al., 2016), early-exit networks (Teerapittayanon et al., 2016), mixture of experts (Shazeer et al., 2017), and spatially adaptive normalization (SPADE (Park et al., 2019)). DPM-Solver (Lu et al., 2022) uses adaptive step sizes globally but not per image. To our knowledge, CAFlow is the first work to combine early-exit routing with

flow matching for super-resolution. Unlike prior early-exit approaches that rely on confidence thresholds or fixed exit schedules, our quality-aware classifier is trained on oracle labels derived from per-exit reconstruction quality, enabling principled per-image routing without ground truth at inference. Critically, diffusion-based SR methods such as SR3 (Saharia et al., 2022) require iterative multi-step denoising where each step conditions on the output of the previous, making per-image depth adaptation fundamentally difficult: all steps must complete before any output is available. Flow matching’s single-step formulation uniquely enables early-exit routing because the entire velocity prediction is produced in one forward pass through a graduated backbone, allowing the model to exit at any depth without sacrificing the iterative structure.

Window Self-Attention Building on the multi-head self-attention mechanism (Vaswani et al., 2017) and its adaptation to vision (Dosovitskiy et al., 2021), the Swin Transformer (Liu et al., 2021) introduced Window Multi-head Self-Attention (W-MSA) and its Shifted-Window variant (SW-MSA) for efficient vision processing. SwinIR (Liang et al., 2021a) adapted this for image restoration. Our HybridFiLMBlock integrates window attention into FiLM-conditioned residual blocks, concentrating attention in later exits where global receptive field most benefits quality.

Loss-Aware and Adaptive Timestep Sampling For diffusion models, P2 weighting (Choi et al., 2022) and Min-SNR (Hang et al., 2024) adapt loss weights across timesteps, but these are global schedules. Curriculum learning (Bengio et al., 2009) and self-paced learning (Kumar et al., 2010) schedule training examples by difficulty. Our loss-aware timestep sampler builds on these ideas with a simple exponential moving average (EMA)-based approach that concentrates gradient signal on difficult timesteps without additional neural networks.

3 Method

3.1 Preliminaries: Flow Matching in Rearranged Space

Given a low-resolution (LR) image $\mathbf{x}_{LR} \in \mathbb{R}^{3 \times H \times W}$, we define the starting point $\mathbf{x}_0 = \text{Bicubic}_{\uparrow s}(\mathbf{x}_{LR})$ and the target $\mathbf{x}_1 = \mathbf{x}_{HR}$, where $s=4$ is the scale factor.

Rather than operating in pixel space, we apply pixel-unshuffle (Shi et al., 2016) to map images into a compact rearranged representation:

$$\tilde{\mathbf{x}} = \text{PixelUnshuffle}_s(\mathbf{x}) \in \mathbb{R}^{3s^2 \times \frac{H}{s} \times \frac{W}{s}}. \quad (1)$$

For $s=4$ and 256×256 crops, this yields 48-channel feature maps at 64×64 spatial resolution. This rearrangement reduces spatial dimensions by s^2 , enabling larger batch sizes and avoiding sub-pixel upsampling layers, while being exactly invertible via pixel-shuffle. All flow matching operates in this rearranged space; we omit the tilde in subsequent equations for brevity, reintroducing it in the algorithms where the rearrangement is made explicit.

The linear interpolation path and target velocity are:

$$\mathbf{x}_t = (1-t)\mathbf{x}_0 + t\mathbf{x}_1, \quad \mathbf{v} = \mathbf{x}_1 - \mathbf{x}_0, \quad t \in [0, 1]. \quad (2)$$

A neural network \mathbf{v}_θ is trained to predict the velocity:

$$\mathcal{L}_{\text{vel}} = \mathbb{E}_{t \sim p(t)} [\|\mathbf{v}_\theta(\mathbf{x}_t, \mathbf{x}_0, t) - \mathbf{v}\|_1], \quad (3)$$

where the timestep distribution $p(t)$ is described in Section 3.4. At inference, we evaluate only at $t=0$, directly predicting the residual from bicubic-upsampled LR to HR in a single forward pass. At inference, a single forward pass at $t=0$ yields:

$$\hat{\mathbf{x}}_1 = \mathbf{x}_0 + \mathbf{v}_\theta(\mathbf{x}_0, \mathbf{x}_0, 0), \quad (4)$$

and the HR image is recovered via pixel-shuffle: $\hat{\mathbf{x}}_{HR} = \text{PixelShuffle}_s(\hat{\mathbf{x}}_1)$. In principle, multi-step Euler integration ($\mathbf{x}_{t+\Delta t} = \mathbf{x}_t + \Delta t \cdot \mathbf{v}_\theta$) can also be applied when the velocity field is sufficiently smooth.

3.2 Hybrid Backbone: FlowResNet

The velocity network is FlowResNet, a 16-block residual network (He et al., 2016) with two types of blocks arranged in a graduated schedule (Figure 1).

The base building block follows the Enhanced Deep Residual (EDSR) design (Lim et al., 2017), a pre-activation residual block without batch normalization that avoids removing range flexibility and reduces GPU memory, augmented with FiLM conditioning (Perez et al., 2018) on the timestep t . A sinusoidal embedding of t is projected to per-channel scale and shift parameters:

$$\begin{aligned} \mathbf{h} &= \text{ReLU}(\text{Conv}_{3 \times 3}(\mathbf{x})), \\ (\boldsymbol{\gamma}, \boldsymbol{\beta}) &= \text{Linear}(\text{SiLU}(\mathbf{e}_t)), \\ \mathbf{h} &= \mathbf{h} \odot (1 + \boldsymbol{\gamma}) + \boldsymbol{\beta}, \\ \text{FiLMResBlock}(\mathbf{x}) &= \mathbf{x} + \alpha \cdot \text{Conv}_{3 \times 3}(\mathbf{h}), \end{aligned} \quad (5)$$

where $\alpha=0.1$ is the residual scale and \mathbf{e}_t is the timestep embedding. The second convolution is zero-initialized so that each block starts as an identity function.

For later exits requiring global context, we augment the FiLMResBlock with window self-attention (W-MSA/SW-MSA (Liu et al., 2021; Liang et al., 2021a)) to form the HybridFiLMBlock: W-MSA computes attention within local windows to keep computational cost linear, while

SW-MSA shifts these windows in successive layers to build global context.

$$\begin{aligned} \mathbf{x} &\leftarrow \text{FiLMResBlock}(\mathbf{x}, \mathbf{e}_t), \\ \mathbf{x} &\leftarrow \mathbf{x} + \text{W-MSA}(\text{LN}(\mathbf{x})), \\ \mathbf{x} &\leftarrow \mathbf{x} + \text{MLP}(\text{LN}(\mathbf{x})), \end{aligned} \quad (6)$$

where LN is LayerNorm (Ba et al., 2016), W-MSA uses window size $w=8$, 8 attention heads, and learned relative position bias, and the multi-layer perceptron (MLP) has expansion ratio 2. Consecutive hybrid blocks alternate between standard (shift= 0) and shifted (shift= $w/2$) windows for cross-window information flow.

As shown in Figure 1, of the 16 blocks (indices 0 to 15), blocks at indices {5, 9, 11, 13, 14, 15} are HybridFiLM-Blocks; the remaining 10 are FiLMResBlocks. Four exit points are placed at evenly-spaced intervals after blocks 3, 7, 11, and 15:

- **Exit 0 (blocks 0 to 3):** 4 FiLMResBlocks, 0 hybrid blocks, 3.1 GFLOPs.
- **Exit 1 (blocks 0 to 7):** 7 FiLMRes + 1 hybrid, 6.1 GFLOPs.
- **Exit 2 (blocks 0 to 11):** 9 FiLMRes + 3 hybrid, 9.4 GFLOPs.
- **Exit 3 (blocks 0 to 15):** 10 FiLMRes + 6 hybrid, 13.3 GFLOPs.

The concentration of hybrid blocks in later exits creates a non-linear cost gradient: the E3/E0 ratio is 4.3× rather than the 4.0× expected from uniform blocks. Early exits provide local-only processing (cheap, fast), while later exits progressively add global context (expensive, higher quality).

Each intermediate exit (0 to 2) uses a zero-initialized 3×3 convolution mapping features to $3s^2$ -channel velocity in rearranged space. The final exit (3) uses the global residual connection (i.e., body convolution + tail), giving it access to the full skip connection from the head.

The network input is the 96-channel concatenation $[\tilde{\mathbf{x}}_t; \tilde{\mathbf{x}}_0]$ in rearranged space. The output is a $3s^2=48$ -channel predicted velocity. The model totals 1.90M parameters.

3.3 Quality-Aware Exit Routing

At inference, each image should exit at the shallowest depth that preserves quality. We train a lightweight ExitClassifier to predict the optimal exit from backbone features.

The ExitClassifier is a small MLP applied to features from Exit 0: we perform global average pooling, followed by a fully connected layer ($64 \rightarrow 64$) with Rectified Linear Unit (ReLU) activation, a second fully connected layer ($64 \rightarrow 32$) with Rectified Linear Unit (ReLU) activation, and a final linear projection ($32 \rightarrow 4$) producing logits over

the four exits, totaling $\sim 6\text{K}$ parameters. The key design choice is to route from backbone features (after 4 blocks of processing) rather than raw LR input: the network itself reveals whether the image needs further processing.

During training, for samples with $t < 0.15$ (near-inference conditions), we compute the target-image reconstruction L1 loss at each exit:

$$\ell_e = \|\hat{\mathbf{x}}_1^{(e)} - \mathbf{x}_1\|_1, \quad e \in \{0, 1, 2, 3\}. \quad (7)$$

The oracle label is the earliest exit whose loss is within ε of the best:

$$e^* = \min\{e : \ell_e \leq \min_{e'} \ell_{e'} + \varepsilon\}, \quad \varepsilon = 0.02. \quad (8)$$

This encourages early exit whenever quality is comparable, rather than always selecting the lowest-loss exit (which would bias toward deeper exits).

The classifier is trained with cross-entropy loss on oracle labels. Let $\text{sg}(\cdot)$ denote the stop-gradient operator. Then:

$$\mathcal{L}_{\text{router}} = \text{CE}(\text{ExitClassifier}(\text{sg}(\mathbf{f}_{E0})), e^*), \quad (9)$$

where ‘‘CE’’ denotes the cross-entropy loss function, ‘‘ExitClassifier’’ is the lightweight routing network, and \mathbf{f}_{E0} represents the intermediate feature maps extracted at Exit 0. The stop-gradient ensures the router is trained using a separate optimizer and its gradients do not flow into the backbone. This prevents the routing objective from degrading the main network’s feature quality. At inference time, the classifier predicts exit logits from E0 features, and each image is routed to $\hat{e} = \arg \max(\text{logits})$. Images predicted for Exit 0 skip all subsequent blocks; images predicted for deeper exits continue processing. This dynamic, quality-aware routing mechanism during deployment is outlined in Algorithm 2.

3.4 Loss-Aware Timestep Sampling

Standard flow matching samples $t \sim \mathcal{U}(0, 1)$, giving equal weight to all timesteps. We replace this with a strategy that concentrates gradient signal where the model most needs improvement.

We use a logit-normal base distribution:

$$t = \sigma(u), \quad u \sim \mathcal{N}(\mu, \sigma_t^2), \quad (10)$$

with $\mu = -1.0$ and $\sigma_t = 1.0$, concentrating mass on low-to-mid timesteps where inference-relevant predictions occur (Esser et al., 2024).

Since single-step inference evaluates the model at $t=0$, we dedicate half of each training batch to exact $t=0$ samples, making them equivalent to direct residual prediction. The remaining 50% are drawn from the logit-normal or loss-aware distributions.

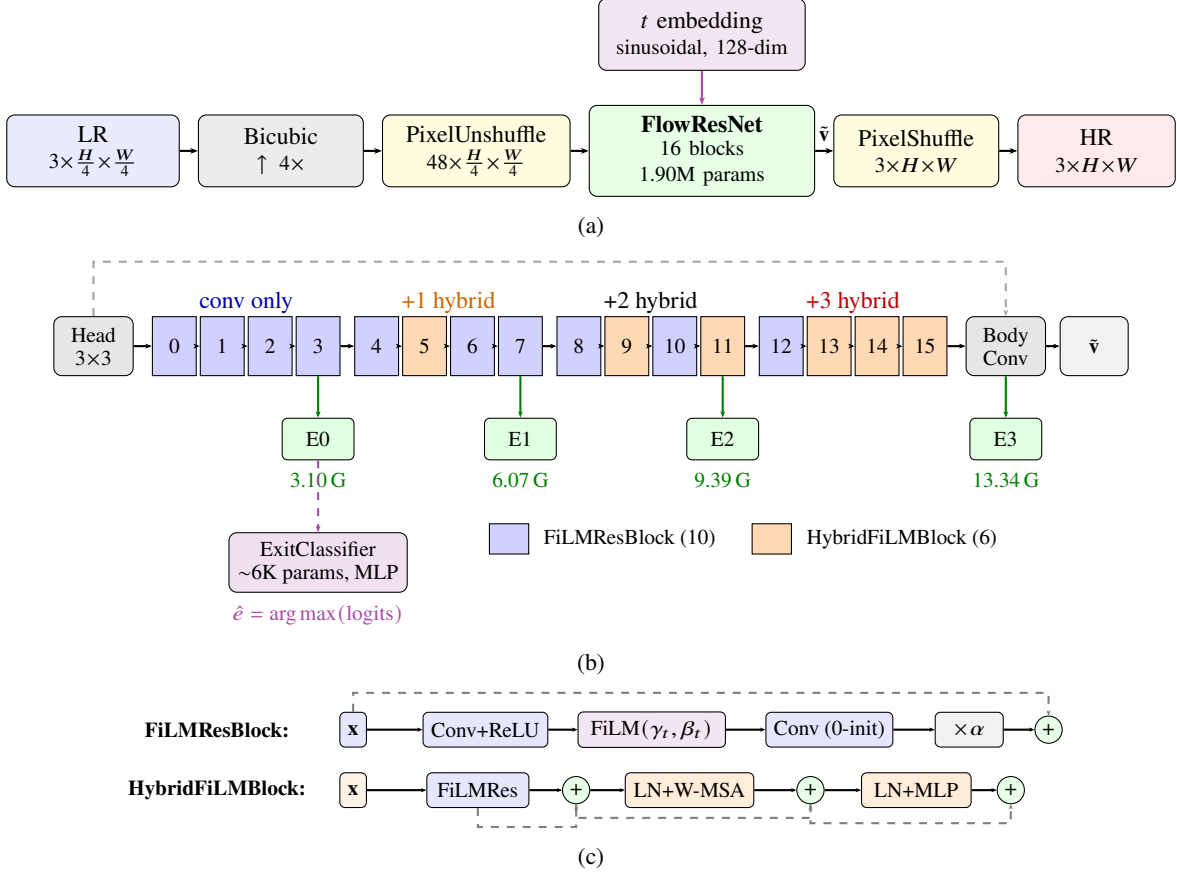


Figure 1: CAFlow architecture overview. (a) The pipeline operates entirely in pixel-unshuffled rearranged space at $\frac{H}{4} \times \frac{W}{4}$ resolution, reducing spatial compute by 16 \times . (b) FlowResNet backbone (1.90M parameters): 16 blocks grouped into 4 exit segments with increasing hybrid (attention) block density, creating a non-linear cost gradient (4.3 \times ratio). The ExitClassifier ($\sim 6\text{K}$ parameters) predicts the optimal exit from E0 features. (c) Internal structure of FiLMResBlock (Eq. 5) and HybridFiLMBlock (Eq. 6). Dashed arrows denote residual connections; HybridFiLMBlock augments the convolutional path with W-MSA/SW-MSA ($w=8$, 8 heads) and a feed-forward MLP.

After warmup, we partition $[0, 1]$ into $B = 20$ equal bins and track the EMA of per-bin velocity losses. After warmup, timesteps are sampled from:

$$p(\text{bin}_b) \propto (1 - \varepsilon) \frac{\ell_b^\alpha}{Z} + \frac{\varepsilon}{B}, \quad (11)$$

where ℓ_b is the EMA loss for bin b , $\alpha = 0.3$ controls sharpness, $\varepsilon = 0.5$ is the uniform mixing ratio, and $Z = \sum_b \ell_b^\alpha$.

3.5 Training Objective and Strategy

During training, all four exits predict velocities and receive equal weight:

$$\mathcal{L}_{\text{multi}} = \frac{1}{4} \sum_{e=0}^3 (\mathcal{L}_{\text{vel}}^{(e)} + \mathcal{L}_{x_0}^{(e)}), \quad (12)$$

where $\mathcal{L}_{\text{vel}}^{(e)} = \|\mathbf{v}_\theta^{(e)} - \mathbf{v}\|_1$ is the velocity L1 loss and $\mathcal{L}_{x_0}^{(e)} = \|\hat{\mathbf{x}}_1^{(e)} - \mathbf{x}_1\|_1$ is the target-image reconstruction loss at exit e , with $\hat{\mathbf{x}}_1^{(e)} = \mathbf{x}_t + (1-t)\mathbf{v}_\theta^{(e)}$.

The Structural Similarity Index Measure (SSIM) loss encourages structural fidelity at the final exit:

$$\mathcal{L}_{\text{SSIM}} = 1 - \text{SSIM}(\hat{\mathbf{x}}_1^{(e_{\text{last}})}, \mathbf{x}_1). \quad (13)$$

The consistency loss enforces that the model predicts the same HR target from different timesteps t_1, t_2 :

$$\mathcal{L}_{\text{consist}} = \|\hat{\mathbf{x}}_1(t_2) - \text{sg}(\hat{\mathbf{x}}_1(t_1))\|_1. \quad (14)$$

The total loss combines these terms:

$$\mathcal{L} = \mathcal{L}_{\text{multi}} + 0.1 \cdot \mathcal{L}_{\text{SSIM}} + 0.1 \cdot \mathcal{L}_{\text{consist}}. \quad (15)$$

The router loss $\mathcal{L}_{\text{router}}$ (Eq. 9) is optimized with a separate optimizer and does not affect backbone gradients.

Algorithm 1 CAFlow Training

1. **Require** FlowResNet \mathbf{v}_θ (4 exits), ExitClassifier C , LossAwareSampler S
 2. **for** epoch = 1, . . . , 700
 3. `is_warmup` \leftarrow (epoch \leq 5)
 4. **for** each batch ($\mathbf{x}_{LR}, \mathbf{x}_{HR}$)
 5. $\tilde{\mathbf{x}}_0 \leftarrow$ PixelUnshuffle(Bicubic \uparrow_4 (\mathbf{x}_{LR}))
 6. $\tilde{\mathbf{x}}_1 \leftarrow$ PixelUnshuffle(\mathbf{x}_{HR})
 7. $t \leftarrow S.sample(epoch)$ \triangleright logit-normal or loss-aware
 8. $\tilde{\mathbf{x}}_t \leftarrow (1-t)\tilde{\mathbf{x}}_0 + t\tilde{\mathbf{x}}_1$
 9. $[\mathbf{v}^{(0)}, \dots, \mathbf{v}^{(3)}], \text{logits, feats} \leftarrow \mathbf{v}_\theta(\tilde{\mathbf{x}}_t, \tilde{\mathbf{x}}_0, t)$
 10. $\mathcal{L} \leftarrow \frac{1}{4} \sum_e (\mathcal{L}_{\text{vel}}^{(e)} + \mathcal{L}_{x_0}^{(e)}) + 0.1 \mathcal{L}_{\text{SSIM}} + 0.1 \mathcal{L}_{\text{consist}}$
 11. Update θ with \mathcal{L} ; update S with per-bin losses
 12. **if** not `is_warmup` **and** $t < 0.15$
 13. $e^* \leftarrow \min\{e : \ell_e \leq \min_{e'} \ell_{e'} + \varepsilon\}$ \triangleright Oracle label
 14. $\mathcal{L}_{\text{router}} \leftarrow CE(\text{logits}, e^*)$
 15. Update C with $\mathcal{L}_{\text{router}}$ \triangleright Separate optimizer
 16. **end if**
 17. **end for**
 18. **end for**
-

Algorithm 2 CAFlow Adaptive Inference

1. **Require** LR image \mathbf{x}_{LR} , FlowResNet \mathbf{v}_θ , ExitClassifier C
 2. $\tilde{\mathbf{x}}_0 \leftarrow$ PixelUnshuffle(Bicubic \uparrow_4 (\mathbf{x}_{LR}))
 3. Process blocks 0 to 3 to obtain E0 features \mathbf{f}_{E0}
 4. $\hat{e} \leftarrow \arg \max(C(\mathbf{f}_{E0}))$ \triangleright Predict optimal exit
 5. **if** $\hat{e} = 0$
 6. $\tilde{\mathbf{v}} \leftarrow \text{ExitHead}_0(\mathbf{f}_{E0})$ \triangleright Skip blocks 4 to 15
 7. **else**
 8. Continue processing blocks 4, . . . up to exit \hat{e}
 9. $\tilde{\mathbf{v}} \leftarrow$ velocity at exit \hat{e}
 10. **end if**
 11. $\hat{\mathbf{x}}_{HR} \leftarrow$ PixelShuffle($\tilde{\mathbf{x}}_0 + \tilde{\mathbf{v}}$)
 12. **return** $\hat{\mathbf{x}}_{HR}$
-

Training proceeds in two phases. In Phase 1 (epochs 1 to 5, warmup), standard flow matching is applied with logit-normal t sampling; the router is not yet trained, and per-bin loss statistics are collected. In Phase 2 (epochs 6 to 700), the router is activated with oracle labels, loss-aware sampling adapts bin probabilities, and all losses are active. We use batch size 32, 256 \times 256 random crops, learning rate 2×10^{-4} with cosine decay, 8-bit AdamW (Loshchilov and Hutter, 2019), bfloat16 mixed precision, and EMA decay 0.9999. The complete end-to-end training procedure is summarized in Algorithm 1.

4 Experiments

4.1 Experimental Setup

We use multi-organ histopathology patches from The Cancer Genome Atlas (TCGA), comprising breast, kidney, and lung tissue. The dataset contains 3,090 training and 343 validation patches at 1024 \times 1024 pixels, including both frozen and permanent section types. During training, we extract random 256 \times 256 crops with horizontal/vertical flip, rotation, and mild color jitter (brightness=0.1, contrast=0.1, saturation=0.05). LR images are generated via $\times 4$ bicubic downsampling.

We compare against the following baselines: Bicubic interpolation; EDSR (Lim et al., 2017) (1.52M parameters, 16.25 GFLOPs) with sub-pixel upsampling; SwinIR-light (Liang et al., 2021a) (0.93M parameters, 8.72 GFLOPs) using the BasicSR implementation; SwinIR-Medium (Liang et al., 2021a) (11.90M parameters, 107.11 GFLOPs), trained from scratch with the same protocol; SRFormer-light (Zhou et al., 2023) (0.87M parameters, 8.25 GFLOPs), a recent transformer baseline using permuted self-attention with window size 16; and SR3 (Saharia et al., 2022), a Denoising Diffusion Probabilistic Models (DDPM)-based diffusion SR model (2.94M parameters) with SDEdit-style initialization, 10 Denoising Diffusion Implicit Models (DDIM) steps \times 4 averaged samples, 4,376 total GFLOPs. Regression baselines (EDSR, SwinIR-light, SwinIR-Medium, SRFormer-light) process at LR resolution with PixelShuffle (Shi et al., 2016) upsampling; SR3 operates at HR resolution (256 \times 256). All baselines are trained from scratch on our dataset with the same optimizer settings.

We report Peak Signal-to-Noise Ratio (PSNR, \uparrow), SSIM (Wang et al., 2004) (\uparrow), and Learned Perceptual Image Patch Similarity (LPIPS, \downarrow) (Zhang et al., 2018a). GFLOPs are measured using PyTorch utilities (FlopCounterMode) at 64 \times 64 LR resolution.

All models are implemented in PyTorch 2.10, RTX 5070 Ti (16 GB), bfloat16 mixed precision, 8-bit AdamW (Loshchilov and Hutter, 2019), learning rate 2×10^{-4} with cosine decay, 700 epochs, batch size 32. FlowResNet: 64 features, 16 blocks, 128-dim time embedding, 4 exits at blocks 3, 7, 11, 15. EMA decay 0.9999.

4.2 Main Results

Table 1 compares CAFlow against baselines on 343 validation patches spanning breast, kidney, and lung tissue. At full depth (Exit 3), CAFlow reaches 31.84 dB PSNR and the highest SSIM (0.8797). SwinIR-Medium matches this PSNR (31.84 dB) and attains slightly lower SSIM (0.8790), but requires 11.90M parameters and 107.11 GFLOPs, compared with 1.90M parameters and

Table 1: Quantitative comparison on multi-organ histopathology $\times 4$ SR (343 validation patches). Best in **bold**, second-best underlined. SR3 GFLOPs reflect total cost of 40 forward passes (10 DDIM steps \times 4 averaged samples).

Method	Params	GFLOPs	PSNR \uparrow	SSIM \uparrow	LPIPS \downarrow
Bicubic	—	—	29.24	0.8096	0.2495
EDSR	1.52M	16.25	31.44	0.8316	0.2003
SwinIR-light	0.93M	8.72	31.76	0.8494	<u>0.1953</u>
SwinIR-Medium	11.90M	107.11	31.84	<u>0.8790</u>	0.1958
SRFormer-light	0.87M	8.25	31.55	0.8718	0.1955
SR3	2.94M	4376	31.39	0.8672	0.1917
CAFlow (Exit 3)	1.90M	13.34	31.84	0.8797	0.1961
CAFlow (Adaptive)	1.90M	8.92	31.72	0.8737	0.1967

13.34 GFLOPs for CAFlow Exit 3. SRFormer-light, a recent ICCV 2023 transformer with permuted self-attention, achieves 31.55 dB PSNR and 0.8718 SSIM with the fewest parameters (0.87M) and comparable GFLOPs to SwinIR-light. With adaptive routing, CAFlow maintains 31.72 dB at only 8.9 GFLOPs, comparable to both SwinIR-light (8.72 GFLOPs) and SRFormer-light (8.25 GFLOPs), while achieving substantially higher structural similarity (SSIM +0.024 over SwinIR-light, +0.002 over SRFormer-light). The 33% compute savings versus full-depth processing come at a cost of only 0.12 dB PSNR, demonstrating that the router effectively identifies images where full depth is unnecessary. On LPIPS, SR3 remains best (0.1917); among the regression baselines, SwinIR-light (0.1953) and SwinIR-Medium (0.1958) are slightly ahead of CAFlow Exit 3 (0.1961), while CAFlow retains the strongest compute-quality tradeoff.

SR3 uses SDEdit-style initialization (noisy bicubic at $t=200$) with 10 DDIM steps and 4-sample averaging, totaling 40 forward passes at full HR resolution (4,376 GFLOPs). This yields competitive distortion metrics (31.39 dB PSNR) and the best LPIPS (0.1917), consistent with diffusion models’ strength in perceptual quality (Saharia et al., 2022). However, this comes at $\sim 490\times$ the compute of CAFlow (Adaptive, 8.92 GFLOPs), which achieves higher PSNR (+0.33 dB) and SSIM (+0.007). CAFlow thus achieves superior distortion quality at a fraction of SR3’s compute cost, validating the efficiency of single-step flow matching with adaptive depth routing. Moreover, SR3 operates at full HR resolution (256 \times 256, 6 channels), whereas CAFlow processes in pixel-unshuffled rearranged space (64 \times 64, 48 channels), yielding a substantially smaller memory footprint (see Table 2).

All pairwise differences are assessed via paired Wilcoxon signed-rank tests over the 343 validation images. CAFlow Exit 3 significantly outperforms EDSR, SRFormer-light, SR3, and SwinIR-light on both PSNR and SSIM ($p < 0.001$ in all cases). Compared to SwinIR-Medium, CAFlow Exit 3 achieves significantly higher

Table 2: Inference efficiency on a single RTX 5070 Ti (16 GB), bfloat16, batch 1, 64 \times 64 LR input ($\times 4$ SR). Latency averaged over 200 runs after 20 warmup passes. Best learned method per metric in **bold**.

Method	Params	GFLOPs	ms	img/s	VRAM
Bicubic	—	—	0.9	1,125	2
EDSR	1.52M	16.25	20.8	48	30
SwinIR-light	0.93M	8.72	60.1	17	99
SwinIR-Medium	11.90M	107.11	84.1	12	129
SRFormer-light	0.87M	8.25	44.9	22	106
SR3	2.94M	4,376	1,082.1	1	145
CAFlow (E0)	1.90M	3.10	2.4	418	22
CAFlow (E1)	1.90M	6.07	4.7	211	43
CAFlow (E2)	1.90M	9.39	8.2	122	47
CAFlow (E3)	1.90M	13.34	12.4	80	49
CAFlow (Adp)	1.90M	8.92	8.2	122	46

SSIM ($p < 0.01$) and statistically indistinguishable LPIPS ($p = 0.82$), while matching PSNR to two decimal places in Table 1 at 8 \times fewer GFLOPs. The adaptive quality cost (-0.12 dB PSNR, -0.006 SSIM vs. full depth) is statistically significant ($p < 0.001$) but practically small, representing the price of a 33% compute reduction; the corresponding measured latency reduction is 34% (Section 4.3).

4.3 Inference Efficiency

Table 2 reports wall-clock latency and peak GPU memory measured on a single RTX 5070 Ti with bfloat16 mixed precision and batch size 1. GFLOPs translate to proportional latency gains: CAFlow Exit 0 (2.4 ms) is the fastest learned method, and Exit 3 (12.4 ms) is faster than both SwinIR-light (60.1 ms) and SwinIR-Medium (84.1 ms). Peak GPU memory usage (VRAM) follows the same trend: CAFlow uses 22 to 49 MB across exits versus 99 MB for SwinIR-light, 129 MB for SwinIR-Medium, and 145 MB for SR3, directly reflecting the benefit of operating at 64 \times 64 rearranged resolution rather than 256 \times 256 HR. SR3’s 40 forward passes incur 1,082 ms latency (87 \times slower than CAFlow E3), confirming that GFLOPs savings translate to real wall-clock speedups. Notably, CAFlow E3 is faster than SwinIR-light despite having more GFLOPs (13.34 vs. 8.72), and is 6.8 \times faster than SwinIR-Medium while using roughly 8 \times fewer GFLOPs (13.34 vs. 107.11). The convolution-dominated rearranged-space formulation is memory-bandwidth efficient, whereas SwinIR’s window attention incurs overhead from reshaping, masking, and softmax operations that underutilize GPU compute at small batch sizes. Adaptive routing achieves the same 34% latency reduction predicted by GFLOPs: CAFlow Adaptive processes each tile in 8.2 ms versus 12.4 ms for

Table 3: Per-exit quality and compute breakdown for CAFlow on $\times 4$ SR. Hybrid shows the number of Hybrid-FiLMBlocks processed at each exit.

Exit	Blocks	Hybrid	GFLOPs	PSNR \uparrow	SSIM \uparrow	LPIPS \downarrow
E0	0–3	0	3.10	31.17	0.8625	0.2003
E1	0–7	1	6.07	31.60	0.8717	0.1969
E2	0–11	3	9.39	31.72	0.8740	0.1971
E3	0–15	6	13.34	31.84	0.8797	0.1961
Adaptive	—	—	8.92	31.72	0.8737	0.1967

Exit 3, with the exit classifier routing each tile to its predicted optimal depth at negligible overhead. In a clinical digital pathology pipeline processing hundreds of tiles per whole-slide image, these per-tile latency differences compound: at Exit 3, CAFlow can process a 300-tile slide in ~ 3.7 s versus ~ 325 s for SR3, a difference that determines whether real-time SR is feasible during diagnostic review.

4.4 Per-Exit Analysis

Table 3 shows the per-exit quality and compute breakdown. Quality gains exhibit diminishing returns with depth: the largest gain occurs at E0 \rightarrow E1 (+0.43 dB), while E1 \rightarrow E2 and E2 \rightarrow E3 each contribute only +0.12 dB. Meanwhile, compute increases super-linearly due to the concentration of hybrid attention blocks in later exits: adding the final 4 blocks (E2 \rightarrow E3) costs 3.95 GFLOPs (42% of the full cost) for only 0.12 dB improvement. This asymmetry between quality saturation and compute growth is precisely what motivates adaptive routing.

Notably, Exit 0 alone (3.1 GFLOPs, pure convolution) already exceeds bicubic by +1.93 dB and approaches EDSR quality (31.17 vs. 31.44 dB) at $5.2\times$ less compute, demonstrating that the rearranged-space formulation enables strong baselines even at minimal depth. The adaptive strategy matches Exit 2 quality (31.72 dB) at 5% less compute (8.92 vs. 9.39 GFLOPs), confirming that the router effectively identifies images that do not benefit from the expensive attention blocks in the final segment. This graduated design (pure convolution in the first segment, progressively more attention in later segments) means that the marginal cost of each quality increment increases, giving the router a natural trade-off surface to exploit.

4.5 Ablation Study

Table 4 ablates key components of the full CAFlow model. The most critical factor is $t=0$ mixing (-1.54 dB without it): dedicating half of training to exact $t=0$ samples is essential for single-step inference quality, as the model otherwise lacks direct supervision at the inference timestep. Without $t=0$ mixing, the model is trained predominantly

Table 4: Ablation study on $\times 4$ SR. Each row removes one component from the full CAFlow model. Δ PSNR shows the drop from the full model. Ablations trained for 300 epochs; full model for 700 epochs. Best per metric in **bold**.

Variant	PSNR \uparrow	SSIM \uparrow	LPIPS \downarrow	Δ PSNR
Full CAFlow	31.72	0.8737	0.1967	–
w/o early exit	31.65	0.8742	0.1959	-0.07
w/o consistency	31.55	0.8717	0.1975	-0.17
w/o $t=0$ mixing	30.17	0.8414	0.2175	-1.54
w/o SSIM loss	31.41	0.8680	0.1978	-0.30
Fewer blocks (8)	31.41	0.8677	0.1968	-0.31

on intermediate timesteps ($t > 0$) where the input \mathbf{x}_t already contains partial information about the target; at inference ($t=0$), the model faces a distributional shift since the input is pure bicubic with no target content, leading to the large quality drop. This finding has practical significance for clinical deployment: since inference always evaluates the model at $t=0$, the training distribution must be aligned with the deployment distribution, making $t=0$ mixing not merely a training heuristic but a necessary condition for reliable single-step flow matching SR.

SSIM loss (-0.30 dB) provides structural supervision that complements the per-pixel L1 velocity loss: L1 alone tends to produce slightly blurred reconstructions, whereas SSIM penalizes degradation of local luminance, contrast, and structural patterns. Fewer blocks (-0.31 dB) demonstrates that the full 16-block depth is necessary; halving to 8 blocks removes all 6 hybrid attention blocks, eliminating the global receptive field needed for long-range structural coherence in complex tissue.

Consistency loss contributes +0.17 dB by encouraging the model to predict the same target image from different timesteps, improving prediction stability. This regularization encourages a smooth velocity field: without it, the model may overfit to specific timestep ranges, producing inconsistent \mathbf{x}_0 predictions that degrade average quality.

Removing the early exit mechanism (forcing all images through full depth) causes only -0.07 dB PSNR change with comparable SSIM and LPIPS, confirming that the multi-exit training strategy introduces no quality penalty at the final exit; the early exits act as auxiliary supervision without degrading the main output. The “w/o early exit” variant achieves marginally better SSIM (0.8742 vs. 0.8737) and LPIPS (0.1959 vs. 0.1967), suggesting that auxiliary exit supervision introduces a slight tension between exit-level and final-output objectives, though the magnitude is negligible ($<0.1\%$). The interplay between $t=0$ mixing and consistency loss is noteworthy: $t=0$ mixing provides direct single-step supervision, while consis-

tency loss regularizes the velocity field at intermediate timesteps, yielding a model that is both accurate at inference time and robust to timestep variation during training.

4.6 Compute-Quality Pareto Frontier

Figure 2 plots PSNR against GFLOPs for CAFlow at each exit and the adaptive operating point, revealing a smooth compute-quality tradeoff. The key finding is that CAFlow provides a much stronger compute-quality tradeoff than the fixed baselines: even the cheapest Exit 0 (31.17 dB, 3.1 GFLOPs) approaches EDSR quality (31.44 dB, 16.25 GFLOPs) at 5.2 \times less compute, while Exit 1 (31.60 dB, 6.1 GFLOPs) surpasses both EDSR and SRFormer-light (31.55 dB, 8.25 GFLOPs) at less compute. The adaptive operating point (31.72 dB, 8.9 GFLOPs) achieves quality on par with SwinIR-light (31.76 dB, 8.72 GFLOPs) and surpasses SRFormer-light at comparable compute, but with substantially higher SSIM (0.8737 vs. 0.8494 and 0.8718, respectively). SwinIR-Medium reaches comparable full-depth quality (31.84 dB) only at 107.11 GFLOPs, placing it far to the right of the practical operating region covered by CAFlow. This demonstrates that the graduated backbone design, with cheap convolutions for easy images and expensive attention for hard ones, provides a more efficient compute-quality tradeoff than fixed-architecture baselines. The Pareto curve also shows that no single fixed-compute baseline lies on the CAFlow frontier in the low- to moderate-compute regime: EDSR (16.25 GFLOPs) is Pareto-dominated by Exit 1 at 2.7 \times less compute, SRFormer-light (8.25 GFLOPs) is surpassed by Exit 1, and SwinIR-light (8.72 GFLOPs) matches the adaptive point in PSNR but at lower SSIM, confirming the value of adaptive depth allocation over fixed-architecture design.

4.7 Exit Distribution

Figure 3 shows the distribution of predicted exits across the 343 validation images. The classifier learns a non-trivial routing policy: it routes a substantial fraction of images to early exits (E0/E1), where cheap convolution-only processing suffices, while reserving deeper exits (E2/E3) with expensive attention blocks for images with dense cellular structures, complex nuclear morphology, or fine-grained texture that benefit from global receptive field. This distribution yields the aggregate 8.9 GFLOPs compute cost, a 33% reduction versus processing all images at full depth (13.3 GFLOPs). Importantly, the router achieves this saving while sacrificing only 0.12 dB PSNR (31.72 vs. 31.84 dB), confirming that early exits do not degrade quality for the images routed to them. Consistent with this, router predictions fall within one exit of the oracle assignment for 97.1% of validation images, indicating that the

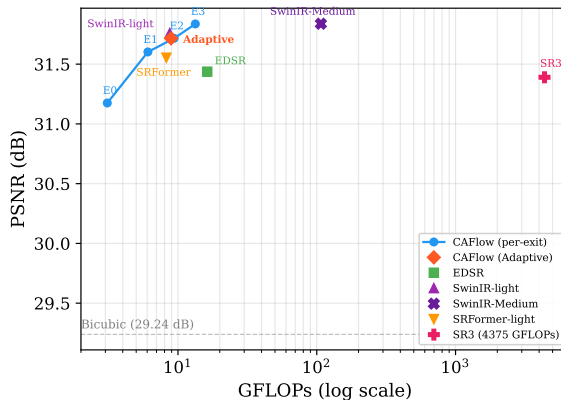


Figure 2: Compute-quality Pareto frontier. CAFlow at different operating points (Exit 0 through Exit 3 and Adaptive) compared against fixed baselines including SwinIR-Medium. The adaptive strategy achieves near-full-depth quality at reduced compute. SwinIR-Medium reaches similar PSNR to CAFlow Exit 3 only at substantially higher compute, while the CAFlow frontier remains stronger in the practical 3.1 to 13.3 GFLOPs regime.

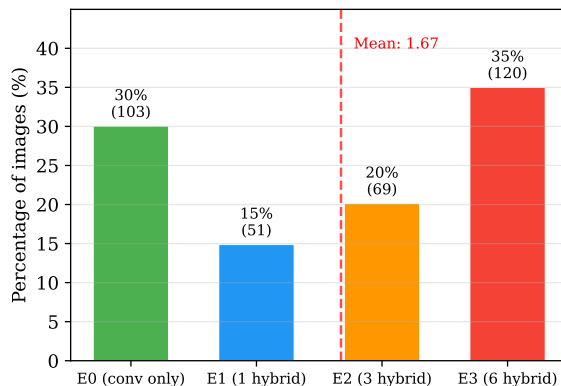


Figure 3: Exit distribution across the 343 validation images under adaptive routing. The classifier routes a mix of images to each exit, with many easy images handled at E0/E1 and harder images pushed to E2/E3.

learned policy is near-oracle even when exact exit labels differ. The classifier’s routing decisions correlate with image content: homogeneous stromal and adipose patches are predominantly routed to E0/E1, while patches containing dense glandular epithelium, heterogeneous staining, or fine-grained nuclear detail are pushed to E2/E3.

4.8 Whole-Slide Tissue Analysis

To demonstrate clinical applicability, we tile a held-out TCGA-BRCA frozen tissue whole-slide image (TCGA-A8-A08C, not present in the training data) at native

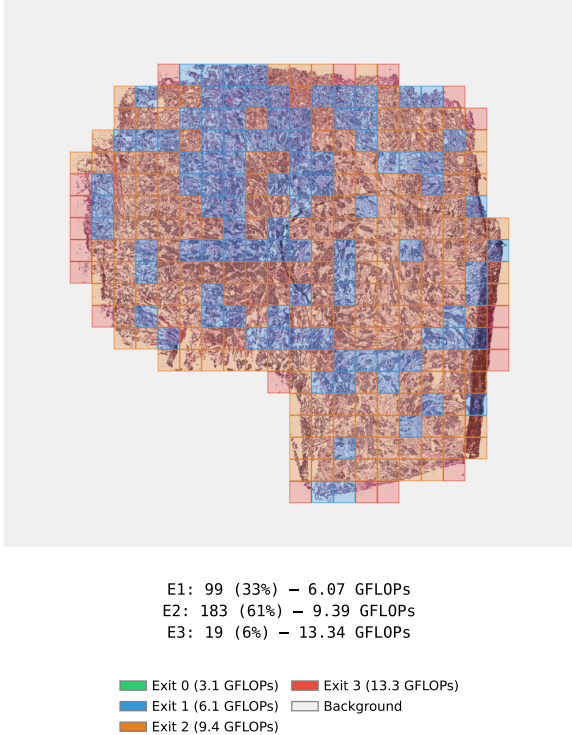


Figure 4: Spatial exit assignment on a held-out TCGA-BRCA frozen tissue slide (TCGA-A8-A08C, not used during training) tiled at $40\times$ into 1024×1024 patches. After tissue detection (Otsu thresholding), 301 tissue tiles are retained and colored by their router-assigned exit: blue (E1, 6.07 GFLOPs), orange (E2, 9.39 GFLOPs), or red (E3, 13.34 GFLOPs). The router assigns 33% to E1 and 61% to E2, with only 6% routed to E3, averaging 8.55 GFLOPs (a 36% reduction versus full-depth processing).

$40\times$ magnification into 1024×1024 patches and apply CAFlow’s exit routing to 301 tissue tiles identified via Otsu thresholding (Figure 4). The resulting spatial exit map reveals spatially coherent routing decisions: the classifier routes 33% of tiles to E1 (6.07 GFLOPs) and 61% to E2 (9.39 GFLOPs), with only 6% assigned to E3 (13.34 GFLOPs), yielding an average cost of 8.55 GFLOPs per tile, a 36% reduction versus full-depth processing. Tiles containing homogeneous tissue content are consistently routed to the shallower E1, while tiles at the boundary between tissue and background, where mixed content creates harder reconstruction targets, are assigned to deeper exits (E2, E3). Notably, this spatial correspondence emerges purely from reconstruction quality signals: the classifier receives no tissue-type labels, no segmentation maps, and no spatial information, yet it learns a routing policy that aligns with tissue complexity as perceived by a pathologist. This result suggests that adaptive

SR routing could serve as a lightweight tissue complexity indicator in whole-slide analysis pipelines. From a deployment perspective, the 36% compute reduction at the slide level translates directly to lower inference cost and faster turnaround in high-throughput digital pathology workflows, where thousands of slides may require processing daily.

4.9 Qualitative Comparison

Figure 5 shows visual comparisons across three tissue types (breast, kidney, lung). On easier stromal and tubular patches (breast, kidney), all learned methods substantially outperform bicubic interpolation, and CAFlow at full depth achieves PSNR comparable to SwinIR-light despite using a fundamentally different generative framework. On the most challenging patch (lung, 23.71 dB bicubic), the dense alveolar structures push all methods below 27 dB, yet CAFlow (26.99 dB) and SwinIR-light (27.00 dB) are virtually tied, demonstrating that flow matching achieves competitive perceptual quality without multi-step diffusion. EDSR tends to over-smooth fine cellular boundaries, particularly in the lung tissue where overlapping alveolar walls require high-frequency detail preservation; the attention blocks in CAFlow’s deeper exits help capture these long-range structural dependencies. SR3 achieves similar PSNR but requires 40 forward passes at HR resolution (4,376 GFLOPs), whereas CAFlow uses a single forward pass at LR resolution (13.3 GFLOPs for full depth, or 8.9 GFLOPs with adaptive routing). SwinIR-Medium also reaches similar full-depth quality, but at 107.11 GFLOPs, making CAFlow substantially lighter than both the heavy transformer and multi-step diffusion alternatives in this qualitative comparison. Importantly, the single-step formulation does not sacrifice perceptual sharpness: across all three tissue types, CAFlow produces edges and textures visually comparable to multi-step SR3, suggesting that flow matching’s direct velocity prediction captures high-frequency details without iterative refinement.

4.10 Per-Organ Analysis

Table 5 reports per-organ metrics with standard deviations across validation patches for breast, kidney, and lung tissue. Performance varies across organs: breast tissue, with relatively homogeneous stromal patterns, achieves the highest PSNR across all methods; kidney tissue, containing fine glomerular structures and tubular boundaries, presents intermediate difficulty; and lung tissue, with dense overlapping alveolar walls and heterogeneous cellular density, is consistently the most challenging. These organ-specific differences are reflected in the standard deviations: lung patches exhibit wider variance in all metrics, reflecting the greater diversity of tissue structures within

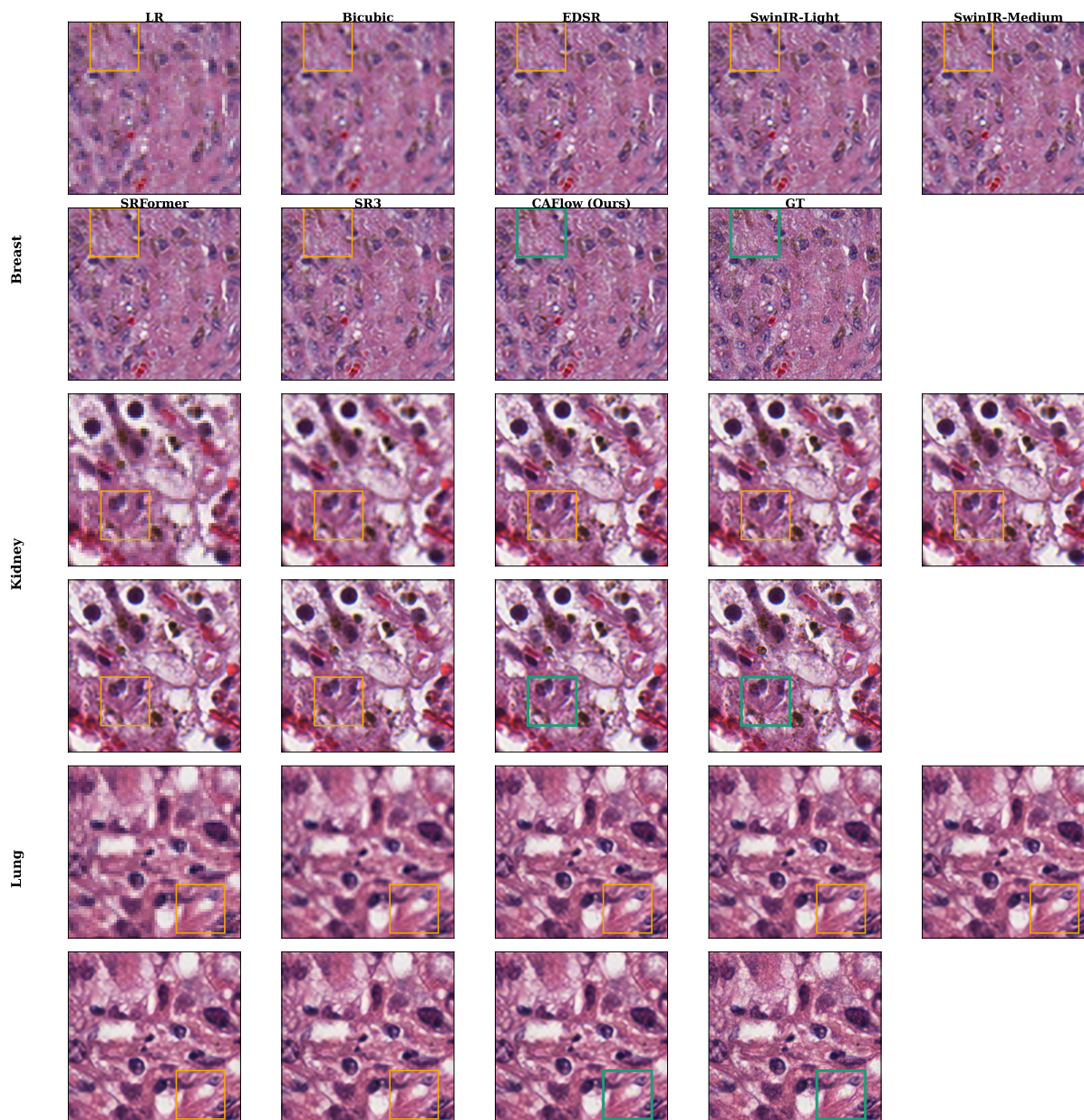


Figure 5: Qualitative comparison on $\times 4$ histopathology SR across breast, kidney, and lung tissue. All examples are taken from the deterministic validation split, using organ-specific patches with highlighted ROIs. Colored boxes mark structures where CAFlow preserves clearer or competitive nuclear separation, lumen definition, or alveolar/stromal continuity than competing methods. Across the highlighted ROIs, CAFlow matches SwinIR-Medium in mean PSNR within 0.03 dB (25.61 vs. 25.63 dB) while achieving higher mean SSIM (0.760 vs. 0.751). Although SwinIR-Medium and SR3 can be visually competitive, they are roughly one to two orders of magnitude heavier in compute and memory.

Table 5: Per-organ quantitative comparison on multi-organ histopathology $\times 4$ SR. Values are mean \pm std across validation patches per organ. Best in **bold**, second-best underlined.

Method	Breast			Kidney			Lung		
	PSNR \uparrow	SSIM \uparrow	LPIPS \downarrow	PSNR \uparrow	SSIM \uparrow	LPIPS \downarrow	PSNR \uparrow	SSIM \uparrow	LPIPS \downarrow
Bicubic	30.64 ± 4.41	0.8331 ± 0.0928	0.2293 ± 0.0523	27.35 ± 5.76	0.7777 ± 0.0957	0.2765 ± 0.0686	27.80 ± 3.92	0.7932 ± 0.0867	0.2639 ± 0.0527
EDSR	32.97 ± 4.42	0.8834 ± 0.0727	0.1837 ± 0.0506	29.57 ± 5.30	0.8499 ± 0.0734	0.2204 ± 0.0642	30.13 ± 4.06	0.8574 ± 0.0659	0.2138 ± 0.0525
SwinIR-light	33.23 ± 4.40	0.8883 ± 0.0701	0.1808 ± 0.0496	30.05 ± 5.37	0.8611 ± 0.0675	0.2148 ± 0.0586	30.46 ± 3.97	0.8650 ± 0.0627	0.2099 ± 0.0511
SwinIR-Medium	33.39± 4.40	<u>0.8913± 0.0687</u>	<u>0.1789± 0.0497</u>	30.27± 5.33	0.8665± 0.0647	0.2165 ± 0.0579	30.66± 4.04	<u>0.8691± 0.0611</u>	0.2099 ± 0.0513
SRFormer-light	33.04 ± 4.36	0.8852 ± 0.0714	0.1812 ± 0.0494	29.84 ± 5.39	0.8559 ± 0.0706	<u>0.2125± 0.0605</u>	30.26 ± 3.92	0.8611 ± 0.0639	<u>0.2088± 0.0510</u>
SR3	32.95 ± 4.50	0.8824 ± 0.0745	0.1772± 0.0462	29.63 ± 5.46	0.8498 ± 0.0737	0.2074± 0.0539	30.09 ± 4.14	0.8554 ± 0.0678	0.2033± 0.0475
CAFlow (E3)	<u>33.29± 4.52</u>	0.8921± 0.0670	0.1799 ± 0.0509	<u>30.08± 5.48</u>	0.8658 ± 0.0646	0.2140 ± 0.0574	<u>30.51± 4.19</u>	0.8698± 0.0598	0.2096 ± 0.0503
CAFlow (Adaptive)	33.15 ± 4.52	0.8864 ± 0.0720	0.1807 ± 0.0511	29.97 ± 5.46	0.8601 ± 0.0669	0.2141 ± 0.0582	30.39 ± 4.20	0.8630 ± 0.0642	0.2102 ± 0.0504

Table 6: Downstream nuclei detection on SR outputs. StarDist (Schmidt et al., 2018) “2D_versatile_he” detects nuclei on each method’s SR output; metrics compare against detections on HR ground truth (IoU threshold = 0.5). All learned SR methods significantly outperform bicubic interpolation; differences among learned methods are not statistically significant (paired t -test, $p > 0.05$), indicating that downstream clinical utility has saturated while computational cost varies widely (Table 2).

Method	Precision \uparrow	Recall \uparrow	Detection F1 \uparrow	Count r \uparrow	Mean IoU \uparrow
Bicubic	0.863 ± 0.152	0.886 ± 0.132	0.869 ± 0.132	0.9799	0.847 ± 0.080
EDSR	0.898 ± 0.127	0.926 ± 0.095	0.905 ± 0.109	0.9878	0.879 ± 0.065
SwinIR-light	0.906 ± 0.122	0.928 ± 0.099	0.911 ± 0.108	0.9886	0.883 ± 0.064
SwinIR-Medium	0.895 ± 0.126	0.936 ± 0.102	0.909 ± 0.111	0.9868	0.884 ± 0.068
SRFormer-light	0.913 ± 0.111	0.916 ± 0.111	0.910 ± 0.101	0.9895	0.885 ± 0.042
SR3	0.901 ± 0.122	0.924 ± 0.100	0.906 ± 0.106	0.9866	0.880 ± 0.065
CAFlow (E3)	0.902 ± 0.130	0.925 ± 0.101	0.906 ± 0.117	0.9888	0.881 ± 0.081
CAFlow (Adaptive)	0.905 ± 0.122	0.925 ± 0.100	0.909 ± 0.107	0.9873	0.882 ± 0.066

the organ.

The adaptive router’s exit distribution also varies by organ (Section 4.7): breast patches are more frequently routed to early exits (E0/E1), consistent with their lower reconstruction difficulty, while lung patches tend to require deeper exits (E2/E3) due to the fine-grained alveolar detail that benefits from the attention layers. Kidney presents a middle ground, with the router distributing images across all exits roughly uniformly. These per-organ routing patterns emerge without any tissue-type supervision, confirming that the quality-aware exit classifier captures intrinsic differences in reconstruction difficulty across anatomical structures.

4.11 Downstream Task Validation

A critical question for clinical deployment of SR in pathology is whether improved pixel-level metrics translate to preserved diagnostic information. To evaluate this, we apply StarDist (Schmidt et al., 2018), a widely-used nuclei

detection model trained on Hematoxylin and Eosin (H&E) histopathology (“2D_versatile_he”), to SR outputs from all methods and compare detected nuclei against detections on HR ground truth images. We match SR detections to HR detections using Intersection over Union (IoU) > 0.5 and report detection F1, Pearson count correlation, and mean IoU of matched nuclei (Table 6).

All learned SR methods significantly outperform bicubic interpolation (F1: 0.87 to 0.90/0.91), confirming that super-resolution preserves diagnostically relevant nuclear structures. Crucially, differences among learned methods are not statistically significant (paired t -test, $p > 0.05$ for all pairwise comparisons), indicating that downstream nuclei detection has saturated: further pixel-metric improvements do not yield measurably better detection. This saturation makes computational efficiency an important differentiator. CAFlow (Adaptive) achieves the same downstream utility as SwinIR-light (F1 = 0.909 vs. 0.911, $p = 0.84$) and matches SwinIR-Medium on detection F1 (0.909 vs. 0.909), while requiring far less compute than the larger transformer baseline (Table 2). All methods achieve high count correlations ($r > 0.987$), with CAFlow (Exit 3) at $r = 0.989$, confirming that the rearranged-space formulation effectively preserves accurate nuclei counts. These results validate CAFlow not merely as a visualization enhancement but as a preprocessing step for automated histopathology analysis pipelines, where efficiency directly impacts whole-slide throughput.

4.12 Cross-Organ Generalization

A key concern for clinical deployment is whether SR models generalize to tissue types unseen during training. To evaluate this, we test all methods on colon tissue (TCGA-COAD, 785 patches), an organ entirely absent from the training set (breast, kidney, lung). Colon tissue is histologically distinct, featuring mucosal crypts, goblet cells, and lamina propria that differ substantially from the glandular, tubular, and alveolar structures in the training organs.

Table 7: Zero-shot cross-organ generalization on held-out colon tissue ($\times 4$ SR). Models trained on breast/kidney/lung, evaluated on entirely unseen colon organ. Best in **bold**, second-best underlined.

Method	PSNR \uparrow	SSIM \uparrow	LPIPS \downarrow
Bicubic	29.58 \pm 4.72	0.8104 \pm 0.0815	0.2469 \pm 0.0595
EDSR	31.49 \pm 4.44	0.8620 \pm 0.0630	0.2030 \pm 0.0579
SwinIR-light	31.75 \pm 4.34	0.8678 \pm 0.0610	0.1994 \pm 0.0564
SwinIR-Medium	31.90\pm4.40	<u>0.8709\pm0.0602</u>	0.1991 \pm 0.0574
SRFormer-light	31.60 \pm 4.30	0.8650 \pm 0.0617	<u>0.1987\pm0.0557</u>
SR3	31.42 \pm 4.54	0.8592 \pm 0.0655	0.1931\pm0.0536
CAFlow (E3)	<u>31.82\pm4.65</u>	0.8719\pm0.0591	0.1993 \pm 0.0576
CAFlow (Adaptive)	31.71 \pm 4.63	0.8659 \pm 0.0625	0.1996 \pm 0.0571

Table 8: Quantitative comparison on multi-organ histopathology $\times 8$ SR. Best in **bold**, second-best underlined.

Method	PSNR \uparrow	SSIM \uparrow	LPIPS \downarrow
Bicubic	24.13 \pm 4.58	0.6149 \pm 0.1538	0.4303 \pm 0.0733
EDSR	25.43 \pm 4.45	0.6684 \pm 0.1410	0.3800 \pm 0.0697
SwinIR-light	25.30 \pm 4.46	0.6616 \pm 0.1399	0.3785 \pm 0.0680
SwinIR-Medium	26.52\pm4.61	0.7105\pm0.1316	0.3555 \pm 0.0711
SRFormer-light	25.23 \pm 4.44	0.6584 \pm 0.1406	0.3820 \pm 0.0678
SR3	25.57 \pm 4.61	0.6728 \pm 0.1430	0.3504\pm0.0659
CAFlow (E3)	<u>26.21\pm4.67</u>	<u>0.7047\pm0.1321</u>	0.3557 \pm 0.0701
CAFlow (Adaptive)	26.14 \pm 4.63	0.6946 \pm 0.1368	<u>0.3532\pm0.0704</u>

Table 7 shows that CAFlow generalizes well to unseen colon tissue: Exit 3 achieves 31.82 dB PSNR and the best SSIM (0.8719), while SwinIR-Medium attains slightly higher PSNR (31.90 dB) at much higher compute. Paired Wilcoxon tests over the 785 colon images confirm that CAFlow Exit 3 significantly outperforms EDSR and SwinIR-light ($p < 0.01$), and remains within 0.09 dB of SwinIR-Medium ($p < 0.001$) at $8\times$ lower compute. The performance gap between training organs (Table 1) and held-out colon is minimal for CAFlow (-0.02 dB PSNR), indicating that the learned representations capture general image reconstruction principles rather than organ-specific features. The adaptive router distributes colon images primarily across intermediate exits (46% E1, 47% E2), treating colon as medium difficulty, a sensible assignment given that colon tissue has moderate structural complexity compared to the heterogeneous lung patches that frequently require deeper exits. SR3 again achieves the best LPIPS (0.1932) on the held-out organ, consistent with its perceptual quality strength observed on training organs.

4.13 Scaling to $\times 8$ Super-Resolution

To evaluate whether CAFlow’s advantages extend to more challenging upscaling factors, we evaluated all methods at $\times 8$ scale (32×32 LR \rightarrow 256×256 HR). All baselines were trained from scratch under the same $\times 8$ protocol; due to its substantially larger cost, SwinIR-Medium was trained for 100 epochs. Table 8 presents the quantitative results and Figure 6 shows representative visual comparisons.

At $\times 8$, CAFlow is especially strong in the practical compute regime. Exit 3 achieves 26.21 dB PSNR and 0.7047 SSIM, outperforming all comparable-compute baselines, including EDSR (16.25 GFLOPs, 25.43 dB), SwinIR-light (8.72 GFLOPs, 25.30 dB), SRFormer-light (8.25 GFLOPs, 25.23 dB), and SR3 (4,376 GFLOPs, 25.57 dB) in PSNR. SwinIR-Medium attains the highest raw distortion metrics at 26.52 dB PSNR and 0.7105 SSIM, but does so with 107.11 GFLOPs, which is about $8.0\times$ the compute of CAFlow Exit 3 (13.34 GFLOPs). Thus, even in this harder $\times 8$ setting, CAFlow remains competitive with a much larger and much more expensive transformer while delivering better quality than all baselines in the low- to moderate-compute regime. Adaptive routing remains effective, with 32% E1, 64% E2, and only 4% E3 exits, achieving 26.14 dB at reduced compute and the second-best LPIPS (0.3532), close to SR3’s 0.3504. This suggests that as the ambiguity of SR increases at $\times 8$, larger-capacity models help, but the flow-matching formulation still scales well: each LR pixel corresponds to 64 HR pixels, yet CAFlow preserves strong reconstruction quality with a single forward pass rather than multi-step denoising.

Figure 6 confirms the quantitative findings visually. At $\times 8$, the lighter regression baselines (EDSR, SwinIR-light, SRFormer-light) produce heavily smoothed outputs that lose fine cellular detail. SwinIR-Medium and CAFlow recover substantially sharper structures, while SR3 restores some texture through iterative denoising but at much higher compute. CAFlow remains visually competitive across all three organs, with particularly clear kidney boundaries, while SwinIR-Medium is the strongest fixed regression baseline in this harder setting.

5 Conclusion

We presented CAFlow, an adaptive-depth flow matching framework for efficient super-resolution that combines three novel components: (1) single-step flow matching in rearranged space, where $t=0$ mixing is essential (-1.54 dB without it); (2) a graduated hybrid backbone with quality-aware routing (1.90M parameters, ~ 6 K classifier) achieving 33% compute savings at 0.12 dB cost; and (3) comprehensive validation including downstream nuclei segmentation, per-organ analysis, cross-organ generalization, and

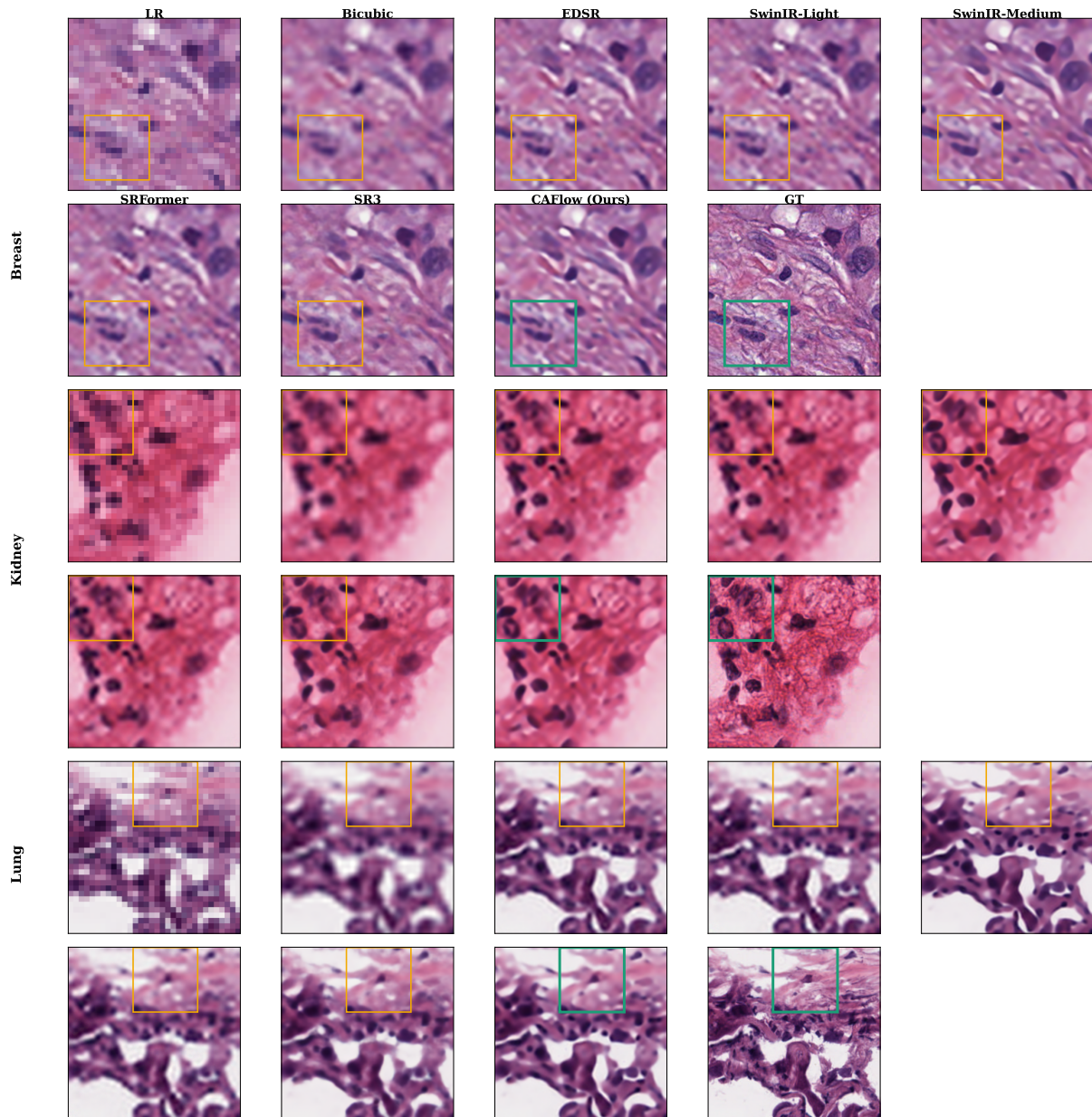


Figure 6: Qualitative comparison on $\times 8$ histopathology SR across breast, kidney, and lung tissue. All examples are taken from the deterministic validation split, using organ-specific patches with highlighted ROIs. Colored boxes mark structures where CAFlow preserves clearer or competitive nuclear separation and boundary continuity than competing methods at this harder scale. Across the highlighted ROIs, CAFlow matches SwinIR-Medium in mean PSNR within 0.03 dB (23.55 vs. 23.57 dB) while achieving higher mean SSIM (0.624 vs. 0.612). Although SwinIR-Medium and SR3 can be visually competitive, they are roughly one to two orders of magnitude heavier in compute and memory.

×8 scaling.

On multi-organ histopathology ×4 SR, CAFlow achieves 31.84 dB PSNR at full depth (13.3 GFLOPs) and 31.72 dB with adaptive routing (8.9 GFLOPs, 33% savings). A much larger SwinIR-Medium reaches similar PSNR only at 107.1 GFLOPs, while CAFlow retains the best SSIM among the x4 methods. The method generalizes to held-out colon tissue with minimal quality degradation (−0.02 dB), and at ×8 remains competitive with a stronger SwinIR-Medium baseline while outperforming all lighter regression baselines. Downstream nuclei segmentation reveals that detection F1 has saturated across learned SR methods ($p > 0.05$), making computational efficiency an important factor for clinical deployment. Although generative SR methods can in principle hallucinate fine-grained structures, CAFlow may reduce this risk through its distortion-oriented objective (L1 + SSIM, no adversarial or perceptual loss), single-step inference that avoids iterative error accumulation, and downstream validation showing that nuclei detection F1 is statistically indistinguishable from HR ground truth. Wall-clock benchmarks confirm that the GFLOPs savings translate to real speedups: CAFlow Exit 3 processes a tile in 12.4 ms (80 img/s) at 49 MB VRAM, compared to 1,082 ms for SR3, 60.1 ms for SwinIR-light, and 84.1 ms for SwinIR-Medium; adaptive routing further reduces latency to 8.2 ms (122 img/s).

Limitations While we demonstrate cross-organ generalization (Section 4.12) and ×8 scaling (Section 4.13), evaluation remains limited to histopathology; generalization to natural images or other medical modalities (radiology, ophthalmology) is untested. The exit classifier is trained on oracle labels derived from L1 loss, which may not perfectly correlate with perceptual quality. Additionally, the current design assumes a fixed number of exits; dynamically adjusting exit placement based on dataset characteristics could further improve efficiency. The batch-size-1 inference regime, common in clinical deployment, does not fully exploit the adaptive routing’s aggregate compute savings; batched inference with mixed-exit assignment would better realize these gains.

Future work Promising directions include scaling to larger backbones with more exit points, extending to other imaging modalities (radiology, ophthalmology), and combining exit routing with knowledge distillation (Hinton et al., 2015) to further compress early exits. Exploring patch-level adaptive depth within a single image, where different spatial regions of a slide tile receive different compute budgets, could enable even finer-grained efficiency. Our downstream nuclei segmentation results suggest that SR-aware loss functions targeting morphological preservation (e.g., detection-based losses) could further

improve clinical utility. Finally, integrating the exit classifier’s tissue complexity signal into downstream analysis tasks (e.g., triaging or quality control) could provide additional clinical value beyond super-resolution.

Acknowledgments

This work was supported by the Israel Ministry of Science and Technology Digital Pathology grant.

References

- E. Abels, L. Pantanowitz, F. Aeffner, M. D. Zarella, et al. Computational pathology definitions, best practices, and recommendations for regulatory guidance: A white paper from the Digital Pathology Association. *Journal of Pathology*, 249(3):286–294, 2019.
- M. S. Albergo and E. Vanden-Eijnden. Building normalizing flows with stochastic interpolants. In *International Conference on Learning Representations (ICLR)*, 2023.
- J. L. Ba, J. R. Kiros, and G. E. Hinton. Layer normalization. *arXiv preprint arXiv:1607.06450*, 2016.
- V. Baxi, R. Edwards, M. Montalto, and S. Saha. Computational pathology: A survey review and the way forward. *Journal of Pathology Informatics*, 15:100357, 2024.
- Y. Bengio, J. Louradour, R. Collobert, and J. Weston. Curriculum learning. In *International Conference on Machine Learning (ICML)*, 2009.
- L. Chen, X. Chu, X. Zhang, and J. Sun. Simple baselines for image restoration. In *European Conference on Computer Vision (ECCV)*, 2022.
- J. Choi, J. Lee, C. Shin, S. Kim, H. Kim, and S. Yoon. Perception prioritized training of diffusion models. In *Proceedings of the IEEE/CVF Conference on Computer Vision and Pattern Recognition (CVPR)*, 2022.
- M. de Haan et al. Deep learning-based transformation of H&E stained tissues into special stains. *Nature Communications*, 12(1):4884, 2021.
- C. Dong, C. C. Loy, K. He, and X. Tang. Learning a deep convolutional network for image super-resolution. In *European Conference on Computer Vision (ECCV)*, 2014.
- A. Dosovitskiy, L. Beyer, A. Kolesnikov, D. Weissenborn, X. Zhai, T. Unterthiner, M. Dehghani, M. Minderer, G. Heigold, S. Gelly, J. Uszkoreit, and N. Houlsby. An image is worth 16×16 words: Transformers for image recognition at scale. In *International Conference on Learning Representations (ICLR)*, 2021.

- P. Esser, S. Kulal, A. Blattmann, R. Entezari, J. Müller, H. Saini, Y. Levi, D. Lorber, F. De Melo, J. Rombach, and R. Rombach. Scaling rectified flow transformers for high-resolution image synthesis. In *International Conference on Machine Learning (ICML)*, 2024.
- T. Hang, S. Gu, C. Li, J. Bao, D. Chen, H. Hu, and Z. Liu. Efficient diffusion training via min-snr weighting strategy. In *International Conference on Learning Representations (ICLR)*, 2024.
- K. He, X. Zhang, S. Ren, and J. Sun. Deep residual learning for image recognition. In *Proceedings of the IEEE/CVF Conference on Computer Vision and Pattern Recognition (CVPR)*, pages 770–778, 2016.
- G. Hinton, O. Vinyals, and J. Dean. Distilling the knowledge in a neural network. *arXiv preprint arXiv:1503.02531*, 2015.
- J. Ho, A. Jain, and P. Abbeel. Denoising diffusion probabilistic models. In *Advances in Neural Information Processing Systems (NeurIPS)*, 2020.
- G. Huang, Y. Sun, Z. Liu, D. Sedra, and K. Q. Weinberger. Deep networks with stochastic depth. In *European Conference on Computer Vision (ECCV)*, pages 646–661, 2016.
- M. P. Kumar, B. Packer, and D. Koller. Self-paced learning for latent variable models. In *Advances in Neural Information Processing Systems (NeurIPS)*, 2010.
- H. Li, Y. Yang, M. Chang, S. Chen, H. Feng, Z. Xu, Q. Li, and Y. Chen. SRDiff: Single image super-resolution with diffusion probabilistic models. *Neurocomputing*, 479:47–59, 2022.
- J. Liang, J. Cao, G. Sun, K. Zhang, L. Van Gool, and R. Timofte. SwinIR: Image restoration using swin transformer. In *ICCV Workshops*, 2021a.
- J. Liang, A. Lugmayr, K. Zhang, M. Danelljan, L. Van Gool, and R. Timofte. Hierarchical conditional flow: A unified framework for image super-resolution and image rescaling. In *Proceedings of the IEEE/CVF International Conference on Computer Vision (ICCV)*, 2021b.
- B. Lim, S. Son, H. Kim, S. Nah, and K. M. Lee. Enhanced deep residual networks for single image super-resolution. In *CVPR Workshops*, 2017.
- Y. Lipman, R. T. Chen, H. Ben-Hamu, M. Nickel, and M. Le. Flow matching for generative modeling. In *International Conference on Learning Representations (ICLR)*, 2023.
- Y. Lipman, M. Havasi, P. Holderrith, N. Shaul, M. Le, V. De Bortoli, R. T. Q. Chen, E. Mathieu, M. Hutchinson, and A. Tong. Flow matching guide and code. *arXiv preprint arXiv:2412.06264*, 2024.
- X. Liu, C. Gong, and Q. Liu. Flow straight and fast: Learning to generate and transfer data with rectified flow. In *International Conference on Learning Representations (ICLR)*, 2023.
- Z. Liu, Y. Lin, Y. Cao, H. Hu, Y. Wei, Z. Zhang, S. Lin, and B. Guo. Swin transformer: Hierarchical vision transformer using shifted windows. In *Proceedings of the IEEE/CVF International Conference on Computer Vision (ICCV)*, 2021.
- I. Loshchilov and F. Hutter. Decoupled weight decay regularization. In *International Conference on Learning Representations (ICLR)*, 2019.
- C. Lu, Y. Zhou, F. Bao, J. Chen, C. Li, and J. Zhu. DPM-Solver: A fast ODE solver for diffusion probabilistic model sampling. In *Advances in Neural Information Processing Systems (NeurIPS)*, 2022.
- T. Park, M.-Y. Liu, T.-C. Wang, and J.-Y. Zhu. Semantic image synthesis with spatially-adaptive normalization. In *Proceedings of the IEEE/CVF Conference on Computer Vision and Pattern Recognition (CVPR)*, 2019.
- E. Perez, F. Strub, H. de Vries, V. Dumoulin, and A. Courville. FiLM: Visual reasoning with a general conditioning layer. In *Proceedings of the AAAI Conference on Artificial Intelligence*, 2018.
- Y. Rivenson et al. Virtual histological staining of unlabelled tissue-autofluorescence images via deep learning. *Nature Biomedical Engineering*, 3(6):466–477, 2019.
- O. Ronneberger, P. Fischer, and T. Brox. U-Net: Convolutional networks for biomedical image segmentation. In *International Conference on Medical Image Computing and Computer-Assisted Intervention (MICCAI)*, pages 234–241, 2015.
- C. Saharia, J. Ho, W. Chan, T. Salimans, D. J. Fleet, and M. Norouzi. Image super-resolution via iterative refinement. *IEEE Transactions on Pattern Analysis and Machine Intelligence*, 45(4):4713–4726, 2022.
- U. Schmidt, M. Weigert, C. Broaddus, and G. Myers. Cell detection with star-convex polygons. In *International Conference on Medical Image Computing and Computer-Assisted Intervention (MICCAI)*, pages 265–273, 2018.

- N. Shazeer, A. Mirhoseini, K. Maziarz, A. Davis, Q. Le, G. Hinton, and J. Dean. Outrageously large neural networks: The sparsely-gated mixture-of-experts layer. In *International Conference on Learning Representations (ICLR)*, 2017.
- W. Shi, J. Caballero, F. Huszár, J. Totz, A. P. Aitken, R. Bishop, D. Rueckert, and Z. Wang. Real-time single image and video super-resolution using an efficient sub-pixel convolutional neural network. In *Proceedings of the IEEE/CVF Conference on Computer Vision and Pattern Recognition (CVPR)*, 2016.
- Y. Song, J. Sohl-Dickstein, D. P. Kingma, A. Kumar, S. Ermon, and B. Poole. Score-based generative modeling through stochastic differential equations. In *International Conference on Learning Representations (ICLR)*, 2021.
- S. Teerapittayanon, B. McDanel, and H.-T. Kung. BranchyNet: Fast inference via early exiting from deep neural networks. In *International Conference on Pattern Recognition (ICPR)*, 2016.
- A. Tong, N. Malkin, G. Huguet, Y. Zhang, J. Rector-Brooks, K. Fatras, G. Wolf, and Y. Bengio. Improving and generalizing flow-based generative models with minibatch optimal transport. *Transactions on Machine Learning Research*, 2024.
- A. Vaswani, N. Shazeer, N. Parmar, J. Uszkoreit, L. Jones, A. N. Gomez, L. Kaiser, and I. Polosukhin. Attention is all you need. In *Advances in Neural Information Processing Systems (NeurIPS)*, 2017.
- J. Wang, E. Yue, Z. Dong, Y. Ma, H. Shan, and J. Wang. Exploiting diffusion prior for real-world image super-resolution. *International Journal of Computer Vision*, 2024.
- X. Wang, K. Yu, S. Wu, J. Gu, Y. Liu, C. Dong, Y. Qiao, and C. Change Loy. ESRGAN: Enhanced super-resolution generative adversarial networks. In *ECCV Workshops*, 2018.
- X. Wang, L. Xie, C. Dong, and Y. Shan. Real-ESRGAN: Training real-world blind super-resolution with pure synthetic data. In *ICCV Workshops*, 2021.
- Z. Wang, A. C. Bovik, H. R. Sheikh, and E. P. Simoncelli. Image quality assessment: From error visibility to structural similarity. *IEEE Transactions on Image Processing*, 13(4):600–612, 2004.
- Z. Wang, J. Chen, and S. C. Hoi. Deep learning for image super-resolution: A survey. *IEEE Transactions on Pattern Analysis and Machine Intelligence*, 43(10):3365–3387, 2020.
- E. Yoshai, G. Goldinger, M. Haifler, and N. T. Shaked. Super-resolution of histopathological frozen sections via deep learning preserving tissue structure. *Advanced Intelligent Systems*, 6(7):2300672, 2024.
- S. W. Zamir, A. Arora, S. Khan, M. Hayat, F. S. Khan, and M.-H. Yang. Restormer: Efficient transformer for high-resolution image restoration. In *Proceedings of the IEEE/CVF Conference on Computer Vision and Pattern Recognition (CVPR)*, 2022.
- R. Zhang, P. Isola, A. A. Efros, E. Shechtman, and O. Wang. The unreasonable effectiveness of deep features as a perceptual metric. In *Proceedings of the IEEE/CVF Conference on Computer Vision and Pattern Recognition (CVPR)*, 2018a.
- Y. Zhang, K. Li, K. Li, L. Wang, B. Zhong, and Y. Fu. Image super-resolution using very deep residual channel attention networks. In *European Conference on Computer Vision (ECCV)*, 2018b.
- Y. Zhou, Z. Li, C. Guo, S. Bai, M. Yang, and Q. Hou. SRFormer: Permuted self-attention for single image super-resolution. In *Proceedings of the IEEE/CVF International Conference on Computer Vision (ICCV)*, 2023.